In Situ Study of Nucleation and Growth Dynamics of Au Nanoparticles on MoS₂ Nanoflakes

Journal:	*Nanoscale*
Manuscript ID	NR-ART-04-2018-003519.R1
Article Type:	Paper
Date Submitted by the Author:	18-Jun-2018
Complete List of Authors:	Song, Boao; University of Illinois at Chicago, Department of Mechanical and Industrial Engineering He, Kun; University of Illinois at Chicago, Mechanical and Industrial Engineering Yuan, Yifei; University of Illinois at Chicago, Mechanical and Industrial Engineering; Argonne National Laboratory, Chemical Science and Engineering Division Sharifi-Asl, Seyyed; University of Illinois at Chicago, Mechanical Engineering Cheng, Meng; University of Illinois at Chicago, Department of Mechanical and Industrial Engineering Lu, Jun; Argonne National Laboratory, Chemical Science and Engineering Division Saidi, Wissam; University of Pittsburgh, Chemical Engineering Shahbazian Yassar, Reza; University of Illinois at Chicago, Department of Mechanical and Industrial Engineering

SCHOLARONE™
Manuscripts

In Situ Study of Nucleation and Growth Dynamics of Au Nanoparticles on MoS$_2$ Nanoflakes

Boao Song [1]*, Kun He* [1]*, Yifei Yuan* [1, 2]*, Soroosh Sharifi-Asl* [1]*, Meng Cheng* [1]*, Jun Lu* [2*]*,*

Wissam A. Saidi [3*]*, Reza Shahbazian-Yassar* [1*]

[1] Department of Mechanical and Industrial Engineering, University of Illinois at Chicago, Chicago,

Illinois 60607, USA

[2] Chemical Science and Engineering Division, Argonne National Laboratory, 9700 S. Cass Avenue,

Argonne, Illinois 60439, USA

[3] Department of Mechanical Engineering and Materials Science, University of Pittsburgh, Pittsburgh,

Pennsylvania 15261, USA

* Correspondence to: rsyassar@uic.edu; alsaidi@pitt.edu; junlu@anl.gov

1

Abstract

Two-dimensional (2D) substrates decorated with metal nanoparticles offer new opportunities to achieve high-performance catalytic behavior. However, little is known on how the substrates control the nucleation and growth processes of the nanoparticles. This paper presents the visualization of dynamic nucleation and growth processes of gold nanoparticles on ultrathin MoS_2 nanoflakes by *in situ* liquid-cell transmission electron microscopy (TEM). The galvanic displacement resulting in Au nuclei formation on MoS_2 was observed in real time inside the liquid cell. We found that the growth mechanism of Au particles on pristine MoS_2 is in between diffusion-limited and reaction-limited, possibly due to presence of electrochemical Ostwald ripening. A larger size distribution and more orientation variation is observed for the Au particles along MoS_2 edge than on interior. Differ from pristine MoS_2, sulfur vacancies on MoS_2 induce Au particle diffusion and coalescence during growth process. Density functional theory (DFT) calculations show that the size difference is because the exposed molybdenum atoms at the edge with dangling bonds can strongly interact with Au atoms, whereas sulfur atoms on MoS_2 interior have no dangling bonds and weakly interact with gold atoms. In addition, S vacancies on MoS_2 generate strong nucleation centers that can promote diffusion and coalescence of Au nanoparticles. The present work provides key insights on the role of 2D materials in controlling the size and orientation of noble metal nanoparticles vital to the design of next generation catalysts.

2

Introduction

Catalytic activity of noble metal particles can be optimized by reducing particle size,[1] increasing surface area[2] and tuning orientation.[3] However, obtaining uniformly distributed noble metal nanoparticles with controllable size, shape, and orientation is remaining as the biggest challenge in catalyst design. Over the last decade, supporting noble metal nanoparticles by various substrates have become a promising route where well-chosen substrates can provide a facile way to limit particle size,[4] control orientation[5] and prevent particle aggregation.[6] Recent advances in large scale synthesis of ultrathin 2D materials have attracted tremendous attention for supporting nanomaterials.[7,8] Besides graphene, many other 2D materials such as transition-metal dichalcogenides (TMDCs) are gaining increased attention since the combination of 2D monolayer form with semiconductor properties.[9] Utilizing TMDCs as templates to grow noble metal nanoparticles opens the possibility of novel composite nanostructures in application of high performance catalyst and electronic devices.[10-13]

The synthesis of noble metal nanoparticles decorated on ultrathin 2D TMDCs has been studied extensively.[14-17] With the help of reducing agents,[15] reducing metal ions from precursors to nanoparticles by chemical reduction is promising because of the relatively low cost and ease of implementation. When the reduction potential of metal ions is more positive compared to the conducting or semiconducting substrate, an electroless deposition called galvanic displacement can occur without any additional reducing agent.[18-20] As an example, when semiconducting MoS_2 is used as substrate, after immersion into aqueous solution containing metal precursors, reduction of metal ions takes place spontaneously by gaining electrons transferred from MoS_2 valence band.[10,14,15] This galvanic displacement reaction allows a straightforward synthesis of 2D composite nanostructures decorated with metal nanoparticles.

3

Furthermore, the ability to precisely control the decoration of metal particles on TMDCs is the subject of current interest.[11,14] Different stabilizers or surface capping agents were added to achieve homogeneously distributed nanoparticles, such as sodium carboxymethyl cellulose[11] and trisodium citrate.[15] Epitaxial growth was also reported for metal nanoparticles such as Pd and Pt that are deposited on MoS_2 with (111) and (101) epitaxial orientations.[15]

Despite that various synthesis strategies for controlling nanoparticles growth on 2D TMDCs are under fast development, the associated mechanism studies mostly relied on theoretical models, which limits an in-depth understanding and exploration of the dynamic essentials. *In situ* (scanning) transmission electron microscopy (S)TEM provides the possibility to directly observe dynamic reaction process in real time with high spatial resolution.[21-28] Benefiting from the design of *in situ* liquid cell consisting of two silicon chips with silicon nitride (SiN) viewing windows, liquid solutions can be stored or flowed between chips without influencing the high vacuum in the (S)TEM chamber. The precise control of the liquid thickness allows sub-nanometer imaging of reactions in liquids or at solid-liquid interfaces.[29] Although several studies showed nanoparticle nucleation and growth in liquid-cell (S)TEM,[30-38] to the best of our knowledge, the nucleation and growth of metal nanoparticles on 2D substrates in the liquid cell has not been investigated. Here, we report a combined *in situ* liquid-cell TEM observation and DFT study of the nucleation and growth processes of Au nanoparticles on MoS_2 nanoflakes. We find that MoS_2 nanoflakes play a vital role in controlling the growth mechanism of Au nanoparticles. Due to electrochemical Ostwald ripening, Au nanoparticles on pristine MoS_2 grow with exponent factor of $\beta \sim 0.41$ which is in between diffusion-limited and reaction-limited mechanism. In contrast, sulfur vacancies on MoS_2 induce Au particle diffusion and coalescence during growth process.

4

Additionally, the nanoparticles nucleating along MoS$_2$ edge have larger size distribution and more orientation variation than those on MoS$_2$ interior. DFT simulations suggest that MoS$_2$ edge is very favorable for Au adsorption due to existence of dangling bonds especially at the Mo-terminated side. In addition, S vacancies generate strong nucleation centers that promote diffusion and coalescence of Au nanoparticles.

Experimental Section

Chemicals. MoS$_2$ powder (<2 μm, 99%, Sigma-Aldrich) and gold chloride AuCl$_3$ (>99.99%, Sigma-Aldrich) were used as received.

MoS$_2$ synthesis and exfoliation. Bulk MoS$_2$ powder was mixed with isopropyl alcohol (IPA) at a concentration of 20 mg/mL. The mixture was sonicated for 5 h in a bath sonicator (Branson 3800, 40kHz, 110W). After that the dispersion was centrifuged at 2000 rpm for 30 min (Thermo Scientific, Legend Micro 21) to remove unexfoliated MoS$_2$. The obtained supernatant was centrifuged at 1500 rpm for 15 min, following by taken out the sediment and re-dispersed in DI water before further characterization.

***Ex situ* deposition of Au nanoparticles on MoS$_2$.** AuCl$_3$ solution was prepared by dissolving powder in DI water with a concentration of 20 mM. 50 μL AuCl$_3$ aqueous solution was added into exfoliated MoS$_2$ dispersion with mild shaking. The resulting solution was sonicated for 5 min before (S)TEM characterization.

In situ **deposition of Au nanoparticles on MoS$_2$.** A liquid flow TEM holder with pair of silicon microchips (Protochips Inc., Raleigh, NC) was used (Figure 1a and b). Each of the microchips has an electron transparent silicon nitride (SiN) viewing window with 50 nm in thickness and $550 \times 20 \ \mu m^2$ in dimension. Spacers with 500 nm thickness (green squares shown in Figure 1a) on one microchip were used to ensure a constant distance between two microchips. The O-rings ensured a liquid cell between two microchips with perfect sealing. One droplet (1 μL) of liquid containing MoS$_2$ dispersion was added on the SiN viewing window of one microchip without touching the surface. To create sulfur vacancies on MoS$_2$, the bottom microchip was placed inside the microscope and irradiated under electron beam in vacuum for 3 min, at a dose rate of 90 $e^-/(Å^2 \cdot s)$. The second microchip was then placed on top of the first one with three screws secured to provide a vacuum sealing. The viewing windows were aligned in parallel to maximize the viewing area.

To flow AuCl$_3$ as precursor into the liquid cell, a microfluid pump was used with Hamilton Syringe containing 1 mL of prepared AuCl$_3$ solution connected to the inlet of PEEK tubing. The microfluid pump was then started with a constant flow rate at 240 $\mu L/hr$. The concentration of Au^{3+} ion was kept the same as it was during *ex situ* experiment. The calculated electron dose rate was approximately 50 $e^-/(Å^2 \cdot s)$ for all *in situ* experiments. Videos were captured using an Orius CCD camera at 30 frames per second with 320×320 resolution. Images were taken with 512×512 scanning resolution. The liquid layer thickness variation due to window bulging effect was calculated using the low-loss EELS data as discussed in Supporting Note S1 and Figure S1 (ESI). To minimize the precursor depletion and confinement effect in the liquid cell, continuous flow of AuCl$_3$ solution is ensured and only MoS$_2$ close

to the window edge was used for this study. However, future studies to analyze the effect of different precursor flow rate are worthwhile to be conducted.

In situ control experiment was performed by presetting imaging condition at a short exposure (0.02s), locate area of interesting, block electron beam and then flow $AuCl_3$ precursor into the holder under same flow rate. Image was taken after five more minutes at same area. Subsequent images were taken with 1 min intervals until no more change is observed.

Electron microscopy characterization. *Ex situ* deposited Au nanoparticles on MoS_2 was characterized by dropping post-reacted solution on lacy copper grid. TEM images were taken by JEOL JEM-3010 operating at 300 kV. The *in situ* liquid cell experiments were carried out inside a spherical aberration corrected JEOL JEM-ARM200CF STEM with a cold field emission source operating at 200 kV. High angle annular dark field (HAADF) images, as well as energy dispersive spectrometer (EDS) spectrum was acquired by the same microscope. TrueMap was used for all EDS signal collection to correct the overlapping of Mo, S, and Au peaks. Electron energy loss spectra (EELS) were acquired on a Gatan GIF Quantum spectrometer with an entrance aperture of 5 mm.

Density Functional Theory Calculations. DFT calculations were performed with a computational setup similar to previous studies.[39-41] The planewave DFT calculations were carried out using VASP 5.2[42] employing the Perdew, Burke, and Ernzerhof (PBE) Generalized Gradient Approximation (GGA)[43] for the exchange-correlation function and projector augmented wave (PAW) pseudopotentials.[44,45] The electronic wavefunctions were expanded with planewaves with energy less than 350 eV. The electronic

self-consistent loop was terminated when energy changes are less than 1×10^{-6} eV and the ionic

relaxations were considered converged when the magnitude of the largest force on any atom is less than

0.01 eV/Å. The $(001)_{MoS2}$ pristine surface and the surface with vacancy was modeled using a 3×3 slab

generated from bulk $(001)_{MoS2}$ with lattice constant of 3.18 Å. The Mo-edge/S-edge of MoS_2 were

modeled using a nanoribbon of 4×4 extension, exposing four Mo/S sites, respectively. To mitigate the

fictitious interactions between the images in the non-periodic directions, we used a supercell approach

with more than 12 Å vacuum. For the S-edge NR we had to increase the vacuum spacing to larger than

25 Å to prevent Au from adsorbing at the Mo edge. The Brillouin zone is sampled using the gamma

point. We allowed all atoms to relax in all models except for the MoS_2 with S vacancy where we fixed

the bottom S layer. Nudge-elastic band (NEB) calculations are carried out to compute the energy

barriers.[46,47] We calculated the nanoparticle binding energy per Au using,

$$E_{BE} = \frac{1}{n}\left(E_{MoS_2+Au_n} - E_{MoS_2} - nE_{Au}\right), \tag{1}$$

where n is the number of Au atoms, $E_{MoS_2+Au_n}$ is the energy of the Au_n/MoS_2 heterostructure in the

optimum geometry, E_{MoS_2} is the energy of the MoS_2 substrate, and E_{Au} is the energy of an isolated Au

atom with $4d^{10}5s^1$ valence according to Hund's rules. The isolated atom was modeled using a large

supercell with a cubic lattice of 15 Å side.

Results and discussion

In this work, *in situ* liquid-cell setup is used to flow $AuCl_3$ solution between two silicon nitride (SiN)

membranes. The schematic of the liquid cell device and its cross-section are shown in Figure 1a and b,

respectively. $AuCl_3$, which is being flowed continuously through the inlet, triggers the following

galvanic displacement reactions once in contact with MoS_2 nanoflakes:

$$Au^{3+} + 3e^- \rightarrow Au^0;$$

$$MoS_2 \rightarrow (MoS_2)^{n+} + ne^-. \tag{2}$$
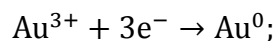
This galvanic displacement takes place spontaneously as the reduction potential (E^o) of Au^{3+}/Au is equal to +1.5V versus the standard hydrogen electrode (SHE)[48], which is below the electron affinity ($\chi = 4.22$ eV)[49] of MoS_2. Therefore, Au^{3+} will be reduced to Au^0 by gaining electrons transferred from MoS_2 substrate.
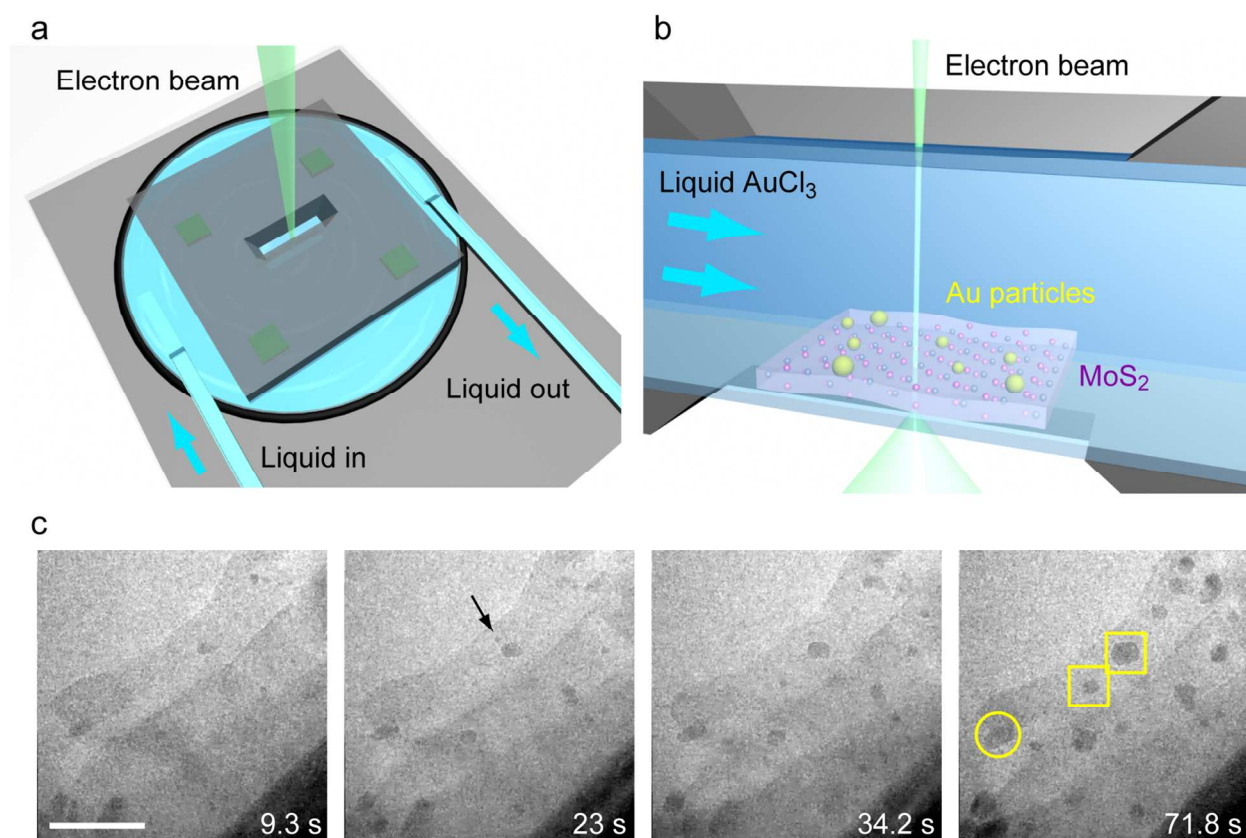

Figure 1. (**a**) The schematic of the liquid-cell (S)TEM device used to study the nucleation and growth of nanoparticles. (**b**) The schematic depicts the reaction happens in liquid cell. (**c**) Snapshots from Movie S1 showing the nucleation and growth of Au nanoparticles on MoS_2 interior (yellow squared regions) and edge (yellow circled region). Scale bar is 50 nm.

9

Movie S1 (Electronic Supplementary Information) shows Au nanoparticles nucleation and growth

on MoS_2 nanoflake. Snapshots from Movie S1 are shown in Figure 1c. As Au^{3+} gains electrons from

MoS_2, gold nuclei began to form on MoS_2 interior (yellow squared regions) and along edge (yellow

circled region). The nuclei grew into larger nanoparticles as time increases, while nucleation happens at

different times and locations. The average particle radius as a function of time is then analyzed and

shown in Figure 2. The radii were calculated based on $(S/\pi)^{1/2}$ where S is the projection area. Detailed

particle detection methodology is included in Supporting Note S2 and Figure S2. Figures 2a and b show

an example of growth profiles of six Au particles that each can be fitted into a power law function in the

form of $R\sim t^\beta$, where β is the mean growth exponent. The classic Lifshitz-Slyozov-Wagner (LSW)

growth theory predicts two growth mechanisms for average radius of particles where β equals to 1/3 and

1/2 for diffusion-limited and reaction-limited models, respectively.[50] Previous *in situ* TEM studies have

shown both consistency[51] and inconsistency[35] compare to the LSW model. Here, the average radius

involving all particles in Movie S1 is shown in Figure 2c, with β determined to be 0.41. Another

example of Au nucleation and growth on MoS_2 (Movie S2) is also analyzed with β equals to 0.42. Since

the two movies are under the same experimental conditions, the results indicate that the growth of Au on

MoS_2 yields an exponent of $\beta \sim 0.41$ which is in between diffusion-limited and reaction-limited growth
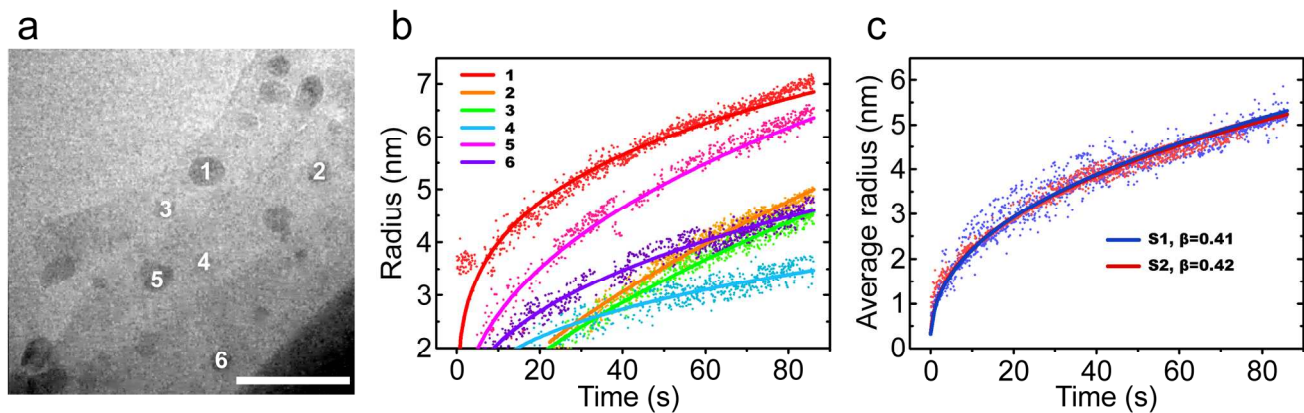
mechanisms predicted by the LSW theory.

10

Figure 2. (**a**) Last frame of Movie S1 where the selected particles are numbered. The scale bar is 50 nm. (**b**) Particle radius as function of time obtained from Movie S1 corresponding to the particles numbered in **a**. (**c**) The average radius as function of time obtained from Movie S1 (blue) and Movie S2 (red).

It is also notable that not all the nanoparticles have continuous size increase upon observation, for instance the small nucleus marked by the black arrow in Figure 1c disappears within a short time after its nucleation. To further understand this, the surrounding areas of two interior particles (squared regions in Figure 1c) and one edge particle (circled region in Figure 1c) were analyzed in Figure 3a, b and c, respectively. The particles marked in yellow outlines are the largest ones in the selected area, while the ones marked by red outlines are nearby smaller particles. We should clarify that the red outlines show only some examples of the particles, and not all of the particles in the image are outlined. In contrast to the growth of the largest particle, the surrounding smaller ones dissolve soon after nucleation, although a successive nucleation of small nuclei at different locations are observed. The similar phenomenon happened both on the interior and edge particles that the largest one grows while surrounding ones dissolve. As there is no coalescence observed for particles on interior or along edge, this growth mechanism can be attributed to the MoS$_2$ substrate-induced electrochemical Ostwald ripening. This is a

11

growth process involving migration of ions and electrons instead of atoms from a smaller particle to a larger particle, when a substrate is present. Brus *et al.*[52] first reported the electrochemical Ostwald ripening phenomenon for silver particles on conductive substrates immersed in water. Their observations suggested that smaller silver particles dissolved by releasing Ag^+ into solution while electrons transferred through the conductive substrate and combined with another ion on larger particles, leading to the continuous growth of the larger one. Later on more studies confirmed that the electrochemical Ostwald ripening phenomenon can take place on semiconducting substrates as well.[53] The electron migration driving force is due to the potential difference between the larger and smaller particles, as smaller particles are easily oxidized.[54] Here, the proposed mechanism is shown in Figure 3d. At stage Ⅰ, the galvanic displacement resulted in nucleation and initial enlargement of the Au nuclei. At stage Ⅱ, the electrochemical Ostwald ripening is triggered due to the potential difference between small and large nuclei. The presence of electrochemical Ostwald ripening may be the reason that Au nanoparticle growth on MoS_2 is bounded by the diffusion-limited and reaction-limited growth mechanisms. To further confirm the electrochemical Ostwald ripening mechanism, more detailed studies utilizing liquid cell setup with better spatial and time resolution are indeed necessary.
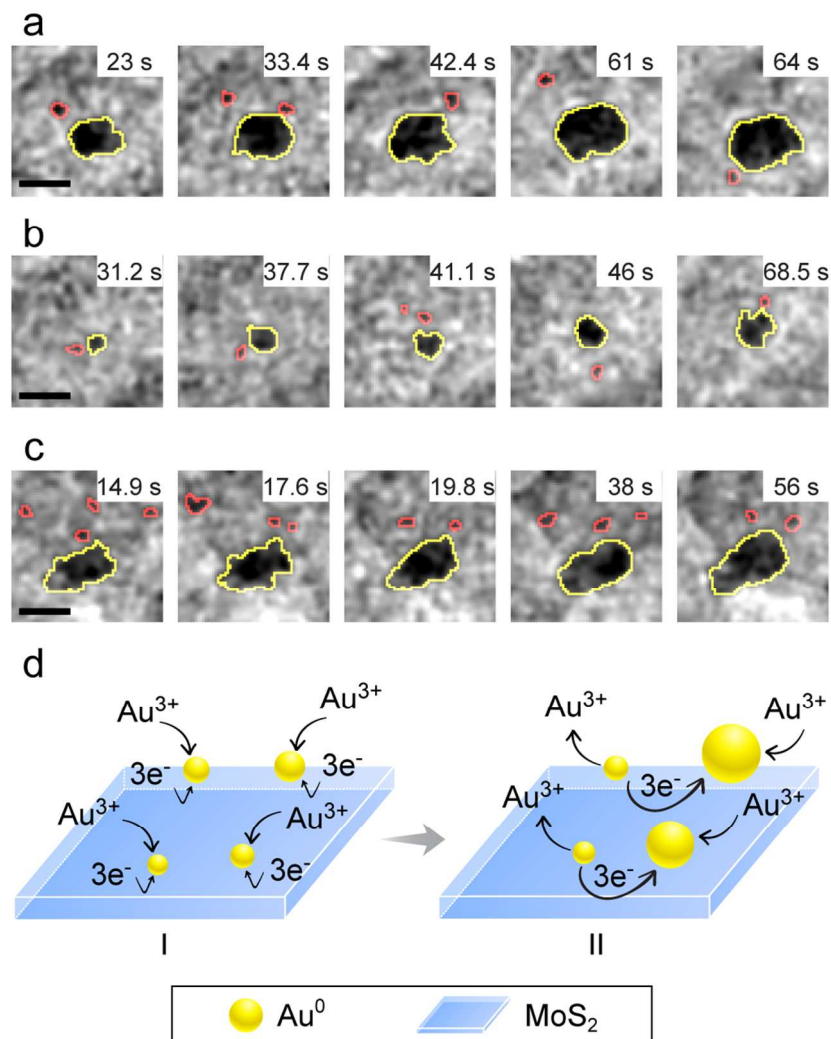
12

Figure 3. (**a-c**) The enlarged surrounding areas of two interior particles (squared regions in Figure 1c) and one edge particle (circled region in Figure 1c). All scale bars are 10 nm. (**d**) The schematic illustration of galvanic displacement of Au^{3+} on MoS_2 (stage Ⅰ) and the following electrochemical Ostwald ripening process (stage Ⅱ).

To better understand this nucleation and growth behavior, the morphology and structure of Au nanoparticles on MoS_2 were further investigated. Figure 4a shows the energy dispersive spectrometer (EDS) mapping of Au nanoparticles that formed on MoS_2. The EDS signals of Si and N from SiN

viewing window are excluded to reduce color interference (see Figure S3 and S4 in ESI for full mapping

and spectrum). Notably, the Au nanoparticles that grow along MoS_2 edge have remarkably larger

diameter compared to those that grow on interior of MoS_2. To quantify the Au nanoparticles size

distribution, HAADF images containing more than 1000 Au nanoparticles formed on MoS_2 were

statistically analyzed. The edges of MoS_2 are further identified by the EELS analysis discussed in

Supporting Note S3 and Figure S5. Figure S6 shows an example image of interior and edge Au

nanoparticles marked by ImageJ.[55] Quantifications of Au nanoparticles size distribution is shown in

Figure 4b. It confirms that the diameter of Au nanoparticles formed on MoS_2 interior ($\approx 7 \pm 4$ nm) is

smaller than that along MoS_2 edge ($\approx 12 \pm 6$ nm). STEM image in Figure 4c shows the uniformly

formed Au particles on MoS_2. The corresponding selected area electron diffraction (SAED) pattern is

shown in the inset. The diffraction spots of $\{100\}_{MoS2}$ can be identified, indicating that the basal plane of

MoS_2 is normal to the electron beam. The inner diffraction ring marked with half dashed circle can be

assigned to $1/3\{422\}_{Au}$ planes and outer diffraction ring is from $\{202\}_{Au}$. Amorphous pattern is

contributed from SiN viewing window. The appearance of $1/3\{422\}_{Au}$ forbidden spots is probably

because the Au thickness along electron pathway is so small that spots from the first Laue zone can be

greatly elongated to intercept with Ewald sphere, especially in the case where the number of $\{111\}_{Au}$

layers is not divisible by three, or due to stacking faults along (111) plane.[15,56] Thereby the zone axis of

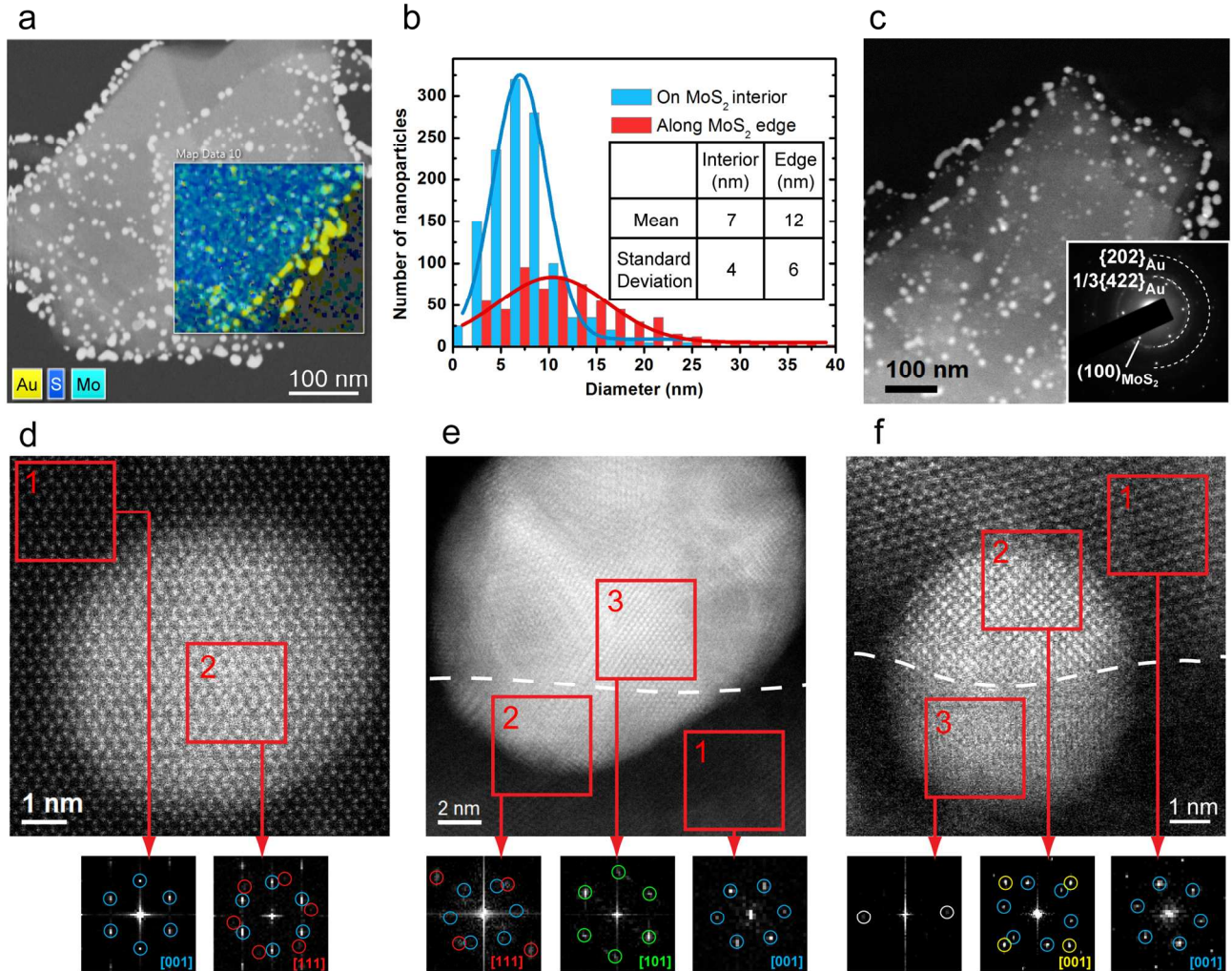Au nanoparticles can be confirmed to <111>.

Figure 4. (**a**) EDS mapping of Au nanoparticles formed on MoS_2. (**b**) Au nanoparticles size distribution and Gaussian fittings. The inset table lists calculated mean and standard deviation of Au nanoparticles diameter. (**c**) HAADF image of *in situ* grown Au nanoparticles on MoS_2. Inset shows the SAED pattern of hexagonal basal plane of MoS_2 along with $1/3\{422\}_{Au}$ and $\{202\}_{Au}$ diffraction rings. (**d**) HAADF image of an Au nanoparticle formed on MoS_2 interior. Two FFT images were taken from the areas marked with red squares. Spots in blue and red circles are from $(001)_{MoS2}$ and $(111)_{Au}$, respectively. (**e**)(**f**) HAADF images of Au nanoparticles formed along MoS_2 edge (indicated by white dashed line). FFT images were taken from the areas marked with red squares. Spots in blue, red, green and yellow circles

are from $(001)_{MoS2}$, $(111)_{Au}$, $(101)_{Au}$, and $(001)_{Au}$, respectively.

The HAADF images of Au nanoparticles formed on MoS_2 interior and along MoS_2 edge are shown in Figure 4d and e-f, respectively. In Figure 4d, Fast Fourier transform (FFT) image from MoS_2 substrate (Region 1) shows the six diffraction spots in blue circles from $(001)_{MoS2}$ basal plane. FFT from Region 2 shows diffraction spots in red circles from $1/3(4\bar{2}\bar{2})_{Au}$, indicating $(111)_{Au}$ orientation. Figure 4e and f show two Au nanoparticles that grown on MoS_2 edge (indicated by white dashed line). Notably, different orientation relationships with MoS_2 basal plane were observed. For instance, Region 3 in Figure 4e where part of Au nanoparticle outside MoS_2 shows diffraction spots in green circles from $(11\bar{1})_{Au}$, $(1\bar{1}\bar{1})_{Au}$ and $(020)_{Au}$, suggesting $(101)_{Au}$ orientation. Figure 4f shows another example of Au with $(001)_{Au}$ atop MoS_2 while no clear zone axis present for the part outside MoS_2. Previous reports have shown that the low-index facets of FCC metal {111} can grow with preferential orientation on MoS_2 surface.[15] One of the reasons is that Au {111} has the lowest surface energy among low Miller index surfaces,[57] which is generally the case for FCC metals.[58-61] Additionally on $(111)_{Au}$ plane the $[1\bar{1}0]_{Au}$ has the smallest lattice mismatch (9.5%) with $[100]_{MoS2}$.[62] Based on our observations, this preferential orientation can be only observed for the Au nanoparticles formed on MoS_2 interior. Au nanoparticles along edge may have several possible orientation relationships with MoS_2 basal plane, with the possible reason that some particles are polycrystals.
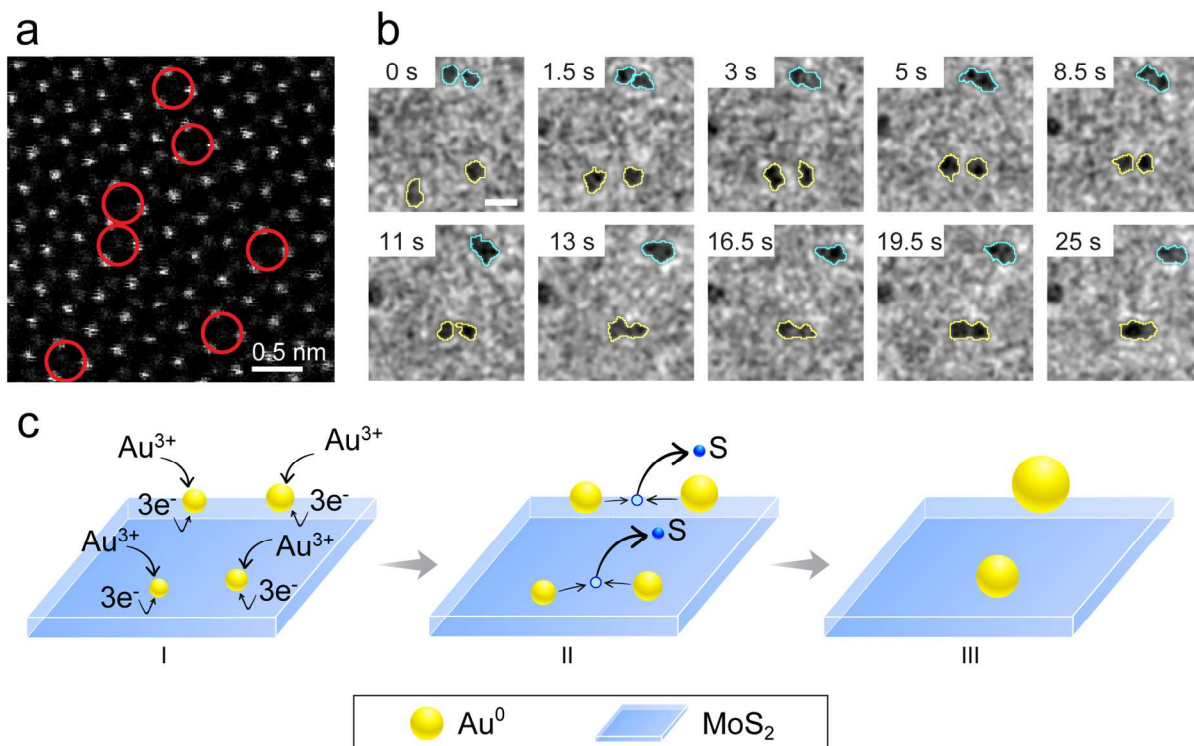
16

Figure 5. (**a**) STEM-HAADF image of MoS$_2$ surface with sulfur vacancies after electron beam irradiation. (**b**) The snapshots from Movie S3 show the dynamics of Au nanoparticles growth on MoS$_2$ with sulfur vacancies. Two pairs of nuclei that migrated and coalesced are outlined by blue and yellow lines. The scale bar is 10 nm. (**c**) The schematic illustration of galvanic displacement of Au^{3+} on MoS$_2$ (stage Ⅰ), diffusion of Au nuclei towards vacancy sites (stage Ⅱ), and particle coalescence mechanism (stage Ⅲ).

In the next step, sulfur vacancies were created on MoS$_2$ nanoflake and the *in situ* TEM experiment was repeated to analyze the effect of vacancies. The effect of electron beam on generating sulfur vacancies is discussed in Supporting Note S4 and Figure S7. Figure 5a shows exemplary HAADF image of sulfur vacancies on MoS$_2$ surface after electron beam irradiation. The lower intensity indicates the

existence of vacancy sites such as the ones marked by red circles. The growth behavior of Au

nanoparticles on the area with sulfur vacancies was recorded in Movie S3 (ESI). The snapshots of Movie

S3 focusing on the vacancy area can be found in Figure 5b. It is interesting that instead of growth into

larger size, the Au nanoparticles have higher mobility to diffuse and coalesce on MoS_2 surface. For

instance, the two nuclei outlined by yellow lines in Figure 5b are well separated at the beginning,

however due to increased diffusion the two nuclei migrate towards each other forming a "neck" at

around 13 s, and finally they coalesce into a larger particle. Similar phenomenon happens for the two

nuclei marked with blue outline. Although galvanic displacement still contributes to the initial

nucleation process, most of the particles stop growing at early growth stage (radii ≤ 3 nm) compare to

the case of pristine MoS_2. In addition, the particle diffusion and coalescence are greatly increased. Based

on the observation, the possible growth mechanism is illustrated in Figure 5c. In stage Ⅰ, the galvanic

displacement induces initial Au nuclei. In stage Ⅱ, S vacancies result in localized midgap states[63] in

MoS_2 electronic structure, and thus induce strong scattering effect.[64] In this circumstance, the galvanic

displacement and electrochemical Ostwald ripening are hindered since scattering effect diminishes the

electron transfer ability. Furthermore, as S vacancies create new favorable adsorption sites for Au nuclei

(see more details in the DFT calculation part), the diffusion towards vacancy sites is greatly enhanced. In

the final stage Ⅲ the surrounding Au particles coalesce into larger ones.

To further verify the nucleation and growth differences of Au nanoparticles on MoS_2 interior, along

edge, and on MoS_2 with S vacancies, DFT calculations are carried out to illustrate the early stages of the

metal adsorption on four different substrate models: 1) pristine MoS_2; 2) MoS_2 nanoribbon (NR) with

Mo-exposed edge; 3) MoS$_2$ NR with S-terminated edge; and 4) MoS$_{2-\eta}$ representing MoS$_2$ with S

vacancies. These models are shown in Figure 6. For each model, we have obtained the optimum

adsorption configuration of 1-4 Au atoms, similar to the previous study of Pt/MoS$_2$ system.[39] The

binding energies of the most stable adsorption configuration are shown in the inset table in Figure 6a.

The adsorption configurations are shown in Figure 6b-6f and Figure S8

For the pristine surface, Au optimum adsorption configuration is atop S site (Figure 6b), which is in

contrast to most metals on MoS$_2$ where the favorable adsorption site with the smallest adsorption energy

is atop Mo site adopting a four coordinated configuration.[40] The binding energy of the Au monomer is

relatively small (0.5-0.6 eV), which is not surprising considering that Au has a deep-lying d-band state

and is relatively inert. The small energy difference (less than 0.1 eV) of the monomer between different

adsorption sites (atop Mo or in the hollow site) suggests a very shallow potential surface for Au

diffusion. This is confirmed with nudged-elastic band (NEB) calculations showing that the Au diffusion

barrier is 0.07 eV. The Au$_2$ dimer (Figure 6c) adopts a configuration where the Au$_2$ bond is perpendicular

to the surface atop S site with a strong binding energy of 1.67 eV/atom. The stability of this

configuration can be understood due to the $4d^{10}5s^1$ valence of isolated Au atom, and the strength of the

Au-Au dimer energy (2.30 eV). Further, the Au-Au bond distance in this vertical configuration is 2.51 Å,

which is similar to that of Au$_2$ dimer of 2.47 Å. In addition to being thermodynamically favorable, NEB

calculations show that two isolated Au atoms can diffuse on the surface and form a dimer without any

kinetic hindrance. These results, in addition to binding energies of Au$_3$ and Au$_4$ in Figure 6a, suggest that

the dimer is the nucleation seed, and large nanoparticles can easily grow on the surface via Au diffusion

and coalescence.

19

Experimentally, it was seen that Au nanoparticles also nucleate along the edge, and the size of the nanoparticles is larger than those that nucleate on MoS_2 interior. To investigate this, we used an MoS_2 NR with exposed Mo and S edges as shown in Figure 6d and e. It was found that the Au adsorption on the Mo-terminated NR is very favorable with an adsorption energy of 3.74 eV/atom. On the other hand, the adsorption of Au on the S-terminated side is less favorable with only 1.8 eV/atom. The difference in bonding of Au to the S-terminated versus Mo-terminated edges can be rationalized by inspecting the bonding configuration. At the Mo edge, Au occupies the bridge site between two neighboring Mo atoms with dangling bonds, while as the bonding on top of sulfur on S-terminated side is not very favorable as sulfur is already bonded to two Mo atoms. Larger Au nanoparticles at the edge site are formed by occupying all available Mo-Mo bridge sites.

Further, we find that the adsorption of Au atop S site on (001) surface near the Mo-terminated edge (~ 1 eV) is less preferable than the edge site but is still larger than the adsorption on (001) surface very far from the edge (~ 0.6 eV). Thus, there is a strong thermodynamic preference for Au nanoparticles to grow at the Mo-terminated MoS_2 edge. Furthermore, it was found that the diffusion of Au from atop site on (001) surface near the Mo-terminated edge to the edge bridge site is barrierless. These results suggest that Au monomers that adsorb on the MoS_2 interior can easily diffuse to the Mo-edge site to nucleate there. In this case, the rate-limiting step is the Au diffusion barrier of 0.07 eV on MoS_2 interior, which is negligible.

For the $MoS_{2-\eta}$ model with one S vacancy (Figure 6f), DFT shows that the Au adsorption passivates the S-vacancy in MoS_2, with very favorable adsorption energy of 2.77 eV. Further the hopping of Au atom from the nearest atop-S adsorption configuration that is close to the vacancy site is barrierless (less

20

than 0.02 eV). Thus, the vacancy site will form a strong nucleation center where the Au nanoparticle can be attracted. As seen experimentally, the high mobility of nanometer scale Au particles can be explained by the low diffusion barrier for constituted Au atoms around vacancy sites.
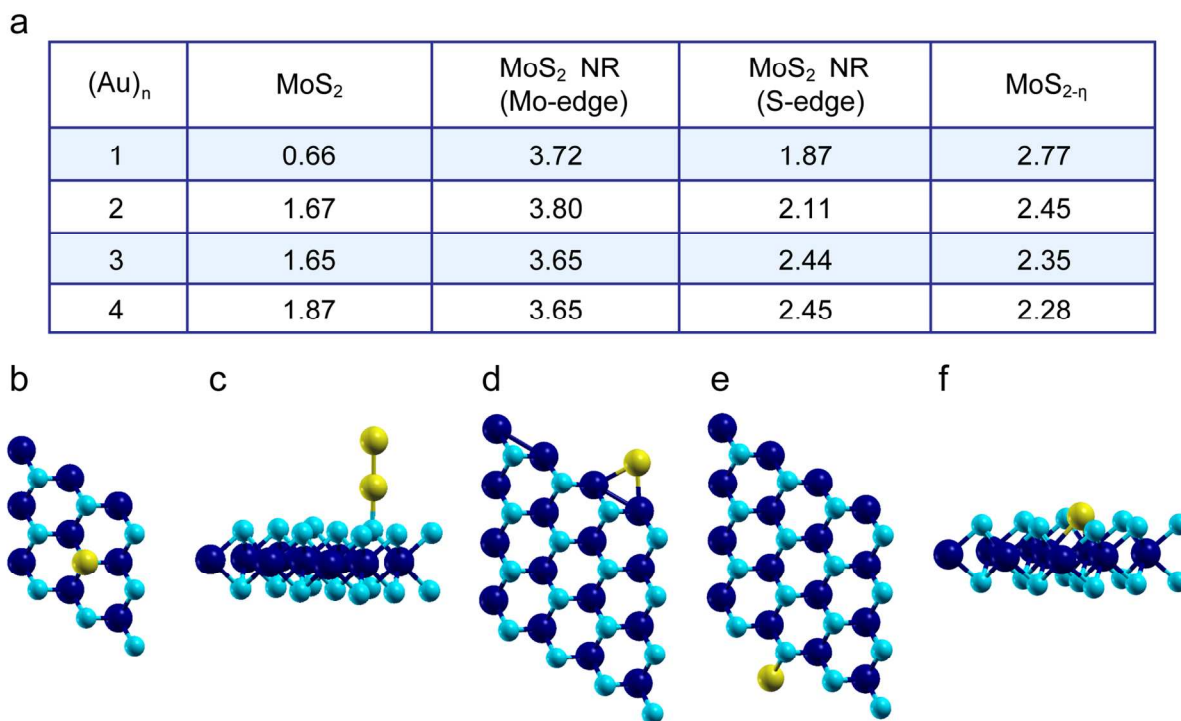
a

$(Au)_n$	MoS_2	MoS_2 NR (Mo-edge)	MoS_2 NR (S-edge)	$MoS_{2-\eta}$
1	0.66	3.72	1.87	2.77
2	1.67	3.80	2.11	2.45
3	1.65	3.65	2.44	2.35
4	1.87	3.65	2.45	2.28

b   c   d   e   f

Figure 6. (**a**) Adsorption energies in eV for 1-4 Au atoms on four different MoS_2 substrates. (**b**) Top view of Au configuration on pristine $(001)_{MoS2}$. (**c**) Side view for dimer Au_2 configuration on $(001)_{MoS2}$. (**d**) and (**e**) are top views of Au configuration on Mo-edge and S-edge of MoS_2 nanoribbon. (**f**) Side view of Au configuration on $(001)_{MoS2-\eta}$ with sulfur vacancy. Mo is shown as dark blue, S as blue, and Au as yellow spheres.

Finally, the role of electron beam was analyzed, and the detailed information is included in Supporting Note S5 and Figure S9. In brief, *ex situ* and *in situ* control experiments were carried out to exclude the influence of electron beam, and the measured Au size distributions were compared with that

21

from *in situ* experiments. It was found that the average particle size both on the edge and interior of MoS$_2$ is slightly smaller in the conditions of *ex situ* and *in situ* control experiments, suggesting that the electron beam may reduce Au^{3+} ions to Au^0 in the liquid cell and trigger the conventional chemical Ostwald ripening. However, the trend that Au particles on MoS$_2$ edge were larger in comparison to the ones on interior remains the same for both *ex situ* and *in situ* conditions. These results also confirm that the nucleation and growth of Au nanoparticles on MoS$_2$ still occur without electron beam, which is consistent with the previous *ex situ* studies.[11,14]

The schematics in Figure 7 summarize the Au nucleation and growth processes on MoS$_2$ nanoflakes based on our observations. The nucleation of Au starts from galvanic displacement of Au ions by accepting electrons from MoS$_2$ nanoflake at initial stage (Figure 7a). Then electrochemical Ostwald ripening is triggered such that the larger nuclei grow even larger by combination of Au ions in solution and electrons transferred from smaller nuclei. Due to the loss of electrons, smaller nuclei dissolve Au ions into solution (Figure 7b). In this growth process, if S vacancies are present on MoS$_2$ surface, electrochemical Ostwald ripening is hindered as the electron transfer pathway will be obstructed by scattering effect. The migration of Au nuclei is then greatly enhanced due to preferable adsorption and low diffusion barriers of the defective S sites. Concomitantly, nuclei with higher surface energy tend to coalesce into larger ones to become more stable (Figure 7c).
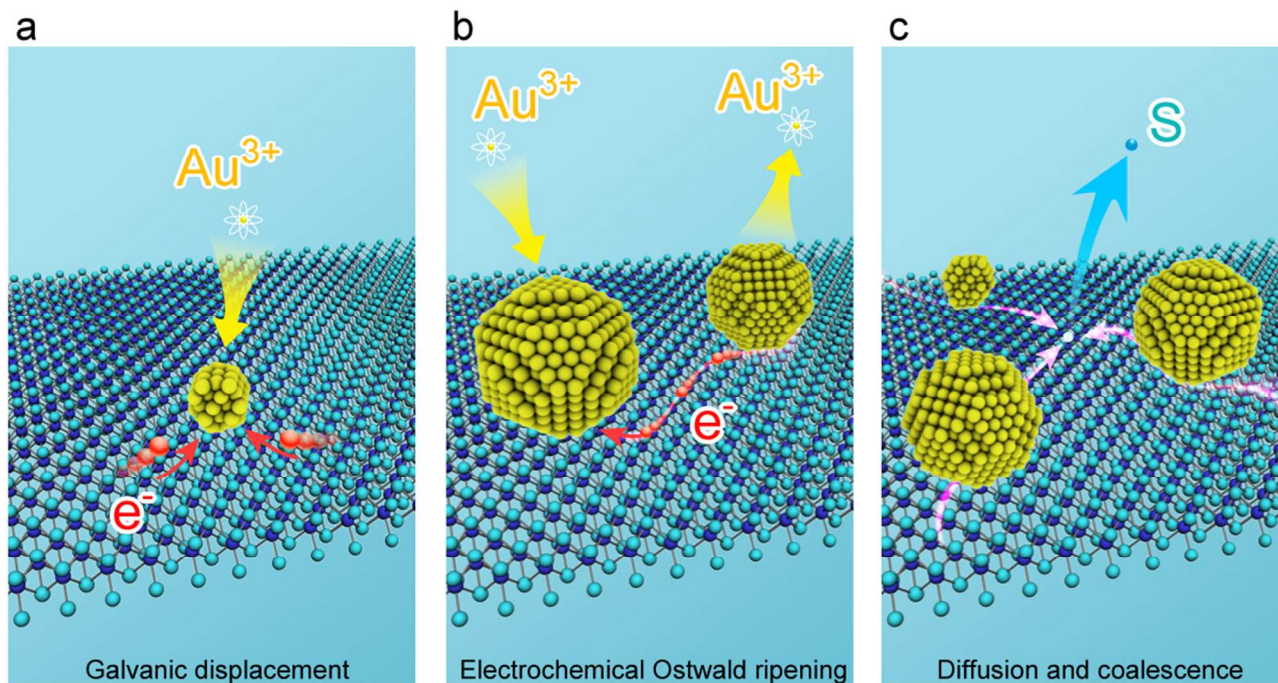
22

Figure 7. Schematic illustration of Au nanoparticles nucleation and growth on MoS_2 nanoflake. (**a**) Galvanic displacement of Au ions to Au nuclei on MoS_2 nanoflake. (**b**) Electrochemical Ostwald ripening process leading to the growth of the larger Au particle and dissolution of smaller Au particle on MoS_2. (**c**) Diffusion and coalescence of Au particles close to S vacancy site.

Conclusions

The present work provides real-time observation of nucleation and growth processes of Au nanoparticles on ultrathin MoS_2 nanoflakes by *in situ* liquid-cell TEM. The galvanic displacement of Au ions to Au nuclei on MoS_2 was observed in real time when $AuCl_3$ flow into the liquid cell. It was found that pristine MoS_2 yield a growth mechanism in between diffusion-limited and reaction-limited model, possibly because of electrochemical Ostwald ripening. The growth of Au nanoparticles on interior of MoS_2 follows oriented attachment on {111} facets considering preferable adsorption. Au nanoparticles formed

along MoS$_2$ edge have a relatively larger size and variety of crystal orientations compared to the ones formed on the interior of MoS$_2$. Differ from pristine MoS$_2$, MoS$_2$ with S vacancies hinder the electrochemical Ostwald ripening but promote diffusion and coalescence. The large difference of Au adsorption energy between edge and interior from DFT calculation explains the tendency of nanoparticles to grow into larger size at MoS$_2$ edge. Furthermore, the generation of vacancies on MoS$_2$ is shown to enhance the coalescence of nanoparticles due to formation of favorable nucleation center at the defective sites. This work shows that *in situ* liquid-cell TEM provides a feasible way to investigate the dynamic nucleation and growth processes of metal nanoparticles on ultrathin substrate. Further, the findings demonstrate how the substrate can affect the growth of deposited metal nanoparticles, and thus shed new insights on the design of substrate-supported catalysts.

Conflicts of interest

There are no conflicts of interest to declare.

Acknowledgments

made use of the JEOL JEM-ARM200CF and JEOL JEM-3010 in the Electron Microscopy Service (Research Resources Center, UIC). The acquisition of the UIC JEOL JEM-ARM200CF was supported by a MRI-R2 grant from the National Science Foundation (Award No. DMR-0959470). We thank Dr. Alan Nicholls and Dr. Fengyuan Shi from UIC for the assistance on (S)TEM results.

Author Contribution

B. Song and R. Shahbazian-Yassar conceived the idea. B. Song carried out the (S)TEM and *in situ* TEM experiments. K. He, Y. Yuan, and S. Sharifi-Asl provided necessary TEM support. W. Saidi carried out the DFT calculations. B. Song and M. Cheng draw the schematic figures. Y. Yuan, W. Saidi and J. Lu provided necessary help in manuscript writing. B. Song wrote the paper under the direction of R. Shahbazian-Yassar. All authors contributed to the discussion and writing of the manuscript.

Electronic Supplementary Information

Electronic Supplementary Information Available. It includes Movie S1, Movie S2, Movie S3, Figure S1-S9, and Supporting Note S1-S5.

25

References

1   A. Salehi-Khojin, H.-R. M. Jhong, B. A. Rosen, W. Zhu, S. Ma, P. J. Kenis and R. I. Masel, *J. Phys. Chem. C*, 2013, **117**, 1627-1632.

2   Q. Lu, J. Rosen, Y. Zhou, G. S. Hutchings, Y. C. Kimmel, J. G. Chen and F. Jiao, *Nat. Commun.*, 2014, **5**, 3242.

3   Y. Yamada, K. Miyamoto, T. Hayashi, Y. Iijima, N. Todoroki and T. Wadayama, *Surf Sci.*, 2013, **607**, 54-60.

4   P. Zhang, Z.-A. Qiao, X. Jiang, G. M. Veith and S. Dai, *Nano Lett.*, 2015, **15**, 823-828.

5   M. A. Hoque, F. M. Hassan, D. Higgins, J. Y. Choi, M. Pritzker, S. Knights, S. Ye and Z. Chen, *Adv. Mater.*, 2015, **27**, 1229-1234.

6   C. Fu, B. Song, C. Wan, K. Savino, Y. Wang, X. Zhang and M. Z. Yates, *Surf. Coat. Technol.*, 2015, **276**, 618-625.

7   C. Tan and H. Zhang, *J. Am. Chem. Soc.*, 2015, **137**, 12162-12174.

8   S. Bai and X. Shen, *RSC Adv.*, 2012, **2**, 64-98.

9   Y. H. Lee, X. Q. Zhang, W. Zhang, M. T. Chang, C. T. Lin, K. D. Chang, Y. C. Yu, J. T. W. Wang, C. S. Chang and L. J. Li, *Adv. Mater.*, 2012, **24**, 2320-2325.

10   J. Kim, S. Byun, A. J. Smith, J. Yu and J. Huang, *J. Phys. Chem. Lett.*, 2013, **4**, 1227-1232.

11   L. Yuwen, F. Xu, B. Xue, Z. Luo, Q. Zhang, B. Bao, S. Su, L. Weng, W. Huang and L. Wang, *Nanoscale*, 2014, **6**, 5762-5769.

12   Z. Yin, B. Chen, M. Bosman, X. Cao, J. Chen, B. Zheng and H. Zhang, *Small*, 2014, **10**, 3537-3543.

13   Y. D. Lampeka and L. V. Tsymbal, *Theor. Exp. Chem.*, 2015, **51**, 141-162.

14   Y. Shi, J. K. Huang, L. Jin, Y. T. Hsu, S. F. Yu, L. J. Li and H. Y. Yang, *Sci. Rep.*, 2013, **3**, 1839.

15   X. Huang, Z. Zeng, S. Bao, M. Wang, X. Qi, Z. Fan and H. Zhang, *Nat. Commun.*, 2013, **4**, 1444.

16   S. Su, C. Zhang, L. Yuwen, X. Liu, L. Wang, C. Fan and L. Wang, *Nanoscale*, 2016, **8**, 602-608.

17   Z. Cheng, B. He and L. Zhou, *J. Mater. Chem. A*, 2015, **3**, 1042-1048.

18   L. A. Porter, H. C. Choi, A. E. Ribbe and J. M. Buriak, *Nano Lett.*, 2002, **2**, 1067-1071.

19   S. Y. Sayed, F. Wang, M. Malac, A. Meldrum, R. F. Egerton and J. M. Buriak, *ACS Nano*, 2009, **3**, 2809-2817.

20   S. M. Alia, Y. S. Yan and B. S. Pivovar, *Catal. Sci. Technol.*, 2014, **4**, 3589-3600.

21   N. de Jonge, D. B. Peckys, G. J. Kremers and D. W. Piston, *Proc. Natl. Acad. Sci. U. S. A.*, 2009, **106**, 2159-2164.

22   N. de Jonge and F. M. Ross, *Nat. Nanotechnol.*, 2011, **6**, 695-704.

23   F. M. Ross, *Science*, 2015, **350**, aaa9886.

24   R. Ramachandramoorthy, R. Bernal and H. D. Espinosa, *ACS Nano*, 2015, **9**, 4675-4685.

25   H. Zheng, Y. S. Meng and Y. Zhu, *MRS Bull.*, 2015, **40**, 12-18.

26   F. Wu and N. Yao, *Nano Energy*, 2015, **11**, 196-210.

27   M. E. Holtz, Y. Yu, D. Gunceler, J. Gao, R. Sundararaman, K. A. Schwarz, T. A. Arias, H. D. Abruna and D. A. Muller, *Nano Lett.*, 2014, **14**, 1453-1459.

28   Z. Zeng, W.-I. Liang, H.-G. Liao, H. L. Xin, Y.-H. Chu and H. Zheng, *Nano Lett.*, 2014, **14**, 1745-1750.

29   K. He, X. Bi, Y. Yuan, T. Foroozan, B. Song, K. Amine, J. Lu and R. Shahbazian-Yassar, *Nano*

27

Energy, 2018, **49**, 338-345.

30 N. D. Loh, S. Sen, M. Bosman, S. F. Tan, J. Zhong, C. A. Nijhuis, P. Kral, P. Matsudaira and U. Mirsaidov, *Nat. Chem.*, 2017, **9**, 77-82.

31 R. R. Unocic, A. R. Lupini, A. Y. Borisevich, D. A. Cullen, S. V. Kalinin and S. Jesse, *Nanoscale*, 2016, **8**, 15581-15588.

32 J. H. Park, N. M. Schneider, J. M. Grogan, M. C. Reuter, H. H. Bau, S. Kodambaka and F. M. Ross, *Nano Lett.*, 2015, **15**, 5314-5320.

33 T. J. Woehl, C. Park, J. E. Evans, I. Arslan, W. D. Ristenpart and N. D. Browning, *Nano Lett.*, 2014, **14**, 373-378.

34 T. J. Woehl, J. E. Evans, I. Arslan, W. D. Ristenpart and N. D. Browning, *ACS Nano*, 2012, **6**, 8599-8610.

35 F. Qin, Z. Wang and Z. L. Wang, *ACS Nano*, 2016, **10**, 9787-9793.

36 A. V. Ievlev, S. Jesse, T. J. Cochell, R. R. Unocic, V. A. Protopopescu and S. V. Kalinin, *ACS Nano*, 2015, **9**, 11784-11791.

37 L. R. Parent, D. B. Robinson, T. J. Woehl, W. D. Ristenpart, J. E. Evans, N. D. Browning and I. Arslan, *ACS Nano*, 2012, **6**, 3589-3596.

38 H. G. Liao, D. Zherebetskyy, H. Xin, C. Czarnik, P. Ercius, H. Elmlund, M. Pan, L. W. Wang and H. Zheng, *Science*, 2014, **345**, 916-919.

39 W. A. Saidi, *Cryst. Growth Des.*, 2015, **15**, 642-652.

40 W. A. Saidi, *Cryst. Growth Des.*, 2015, **15**, 3190-3200.

41 Y. Shi, B. Song, R. Shahbazian-Yassar, J. Zhao and W. A. Saidi, *J. Phys. Chem. Lett.*, 2018, **9**,

2972-2978.

42   G. Kresse and J. Furthmüller, *Phys. Rev. B*, 1996, **54**, 11169-11186.

43   J. P. Perdew, K. Burke and M. Ernzerhof, *Phys. Rev. Lett.*, 1996, **77**, 3865-3868.

44   P. E. Blochl, *Phys. Rev. B*, 1994, **50**, 17953-17979.

45   G. Kresse and D. Joubert, *Phys. Rev. B*, 1999, **59**, 1758-1775.

46   G. Henkelman and H. Jónsson, *J. Chem. Phys*, 2000, **113**, 9978-9985.

47   G. Henkelman, B. P. Uberuaga and H. Jónsson, *J. Chem. Phys.*, 2000, **113**, 9901-9904.

48   D. Lide and W. Haynes, *CRC handbook of chemistry and physics: a ready-reference book of chemical and physical data-/editor-in-chief, David R. Lide; ass. ed. WM" Mickey" Haunes*, Boca Raton, Fla: CRC, 2009.

49   H. Zhong, R. Quhe, Y. Wang, Z. Ni, M. Ye, Z. Song, Y. Pan, J. Yang, L. Yang and M. Lei, *Sci. Rep.*, 2016, **6**, 21786.

50   I. M. Lifshitz and V. V. Slyozov, *J. Phys. Chem. Solids*, 1961, **19**, 35-50.

51   H. Zheng, R. K. Smith, Y. W. Jun, C. Kisielowski, U. Dahmen and A. P. Alivisatos, *Science*, 2009, **324**, 1309-1312.

52   P. L. Redmond, A. J. Hallock and L. E. Brus, *Nano Lett.*, 2005, **5**, 131-135.

53   T. Ghosh, P. Karmakar and B. Satpati, *RSC Adv.*, 2015, **5**, 94380-94387.

54   W. Plieth, *The Journal of Physical Chemistry*, 1982, **86**, 3166-3170.

55   C. A. Schneider, W. S. Rasband and K. W. Eliceiri, *Nat. Methods*, 2012, **9**, 671-675.

56   J. Reyes-Gasga, A. Gomez-Rodriguez, X. Gao and M. Jose-Yacaman, *Ultramicroscopy*, 2008, **108**, 929-936.

29

57   S.-H. Liu, W. A. Saidi, Y. Zhou and K. A. Fichthorn, *J. Phys. Chem. C*, 2015, **119**, 11982-11990.

58   W. A. Saidi, H. Feng and K. A. Fichthorn, *Nano Lett.*, 2012, **12**, 997-1001.

59   W. A. Saidi, H. Feng and K. A. Fichthorn, *J. Phys. Chem. C*, 2013, **117**, 1163-1171.

60   M. Chen, B. Wu, J. Yang and N. Zheng, *Adv. Mater.*, 2012, **24**, 862-879.

61   J. Wu, P. Li, Y.-T. F. Pan, S. Warren, X. Yin and H. Yang, *Chem. Soc. Rev.*, 2012, **41**, 8066-8074.

62   J. Lu, J. H. Lu, H. Liu, B. Liu, L. Gong, E. S. Tok, K. P. Loh and C. H. Sow, *Small*, 2015, **11**, 1792-1800.

63   M. Ghorbani-Asl, A. N. Enyashin, A. Kuc, G. Seifert and T. Heine, *Phys. Rev. B*, 2013, **88**.

64   G. M. Rutter, J. Crain, N. Guisinger, T. Li, P. First and J. Stroscio, *Science*, 2007, **317**, 219-222.

Table of Contents
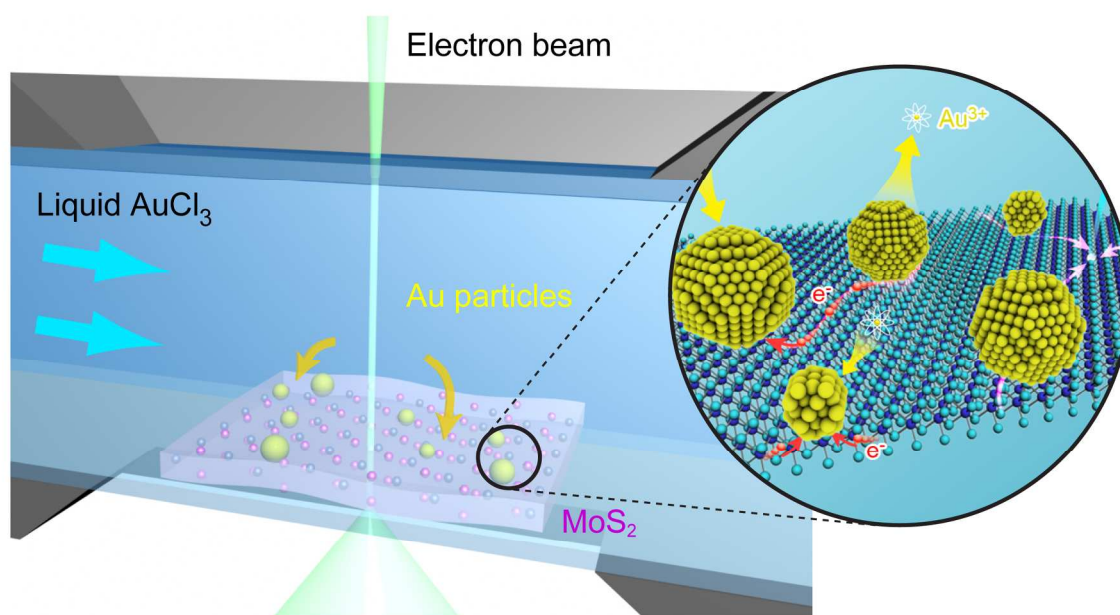
TOC entry. Schematic of the liquid-cell (S)TEM device and the observed nucleation and growth dynamics of Au nanoparticles on MoS_2.